Towards the control of the biological identity of nanobiomaterials: Impact of the structure of 011¯0 surface terminations of nanohydroxyapatite on the conformation of adsorbed proteins

Towards the control of the biological identity of nanobiomaterials: impact of the structure of $\{01\bar{1}0\}$ surface terminations of nanohydroxyapatite on the conformation of adsorbed proteins

Federico Catalano,[a§#] Pavlo Ivanchenko,[a*#] Erica Rebba,[a] Yuriy Sakhno,[a§§] Gabriele Alberto,[a] Galyna Dovbeshko,[b] Gianmario Martra.[a]

[a]Department of Chemistry and Interdepartmental Nanostructured Interfaces and Surfaces (NIS) Centre, University of Torino, via P. Giuria 7, Torino, 10125, Italy

[b]Institute of Physics of the National Academy of Science of Ukraine, 46 Nauky Ave., Kyiv 03028, Ukraine

Keywords: nanohydroxyapatite; surface structure; adsorbed protein; protein conformation; biological identity; IR spectroscopy; CD-UV spectroscopy; zeta-potential

[§]**Present address:** Electron Microscopy Facility, Istituto Italiano di Tecnologia (IIT), via Morego 30, 10163, Genova, Italy.

[§§]**Present address:** Plant & Soil Sciences Department, 154a Townsend Hall, 531 S. College Avenue, Newark, DE 19713, USA.

***Correspondence:** PI: pavlo.ivanchenko@unito.it

[#] FC and PI contributed equally to the work.

ABSTRACT

High-resolution transmission electron microscopy, ζ-potential and in-situ IR spectroscopy of adsorbed CO were combined for elucidating the ratio between $\{01\bar{1}0\}$_Ca-rich:$\{01\bar{1}0\}$_P-rich terminations of $\{01\bar{1}0\}$ facets, i.e. the surfaces with the highest morphological importance, in two nanohydroxyapatite samples. Bovine serum albumin was found to form at least a monolayer on the surface left accessible to protein molecules by the agglomeration of nanoparticles when suspended in the buffered incubation medium. Noticeably, the conformation of adsorbed proteins appeared sensitive to the ratio between the two types of $\{01\bar{1}0\}$ terminations, also resulting in a difference in the surface exposed toward the exterior by the adsorbed protein layer(s).

INTRODUCTION

Hydroxyapatite – $Ca_{10}(PO_4)_6(OH)_2$ (hereafter referred to as HA) is among the most abundant mineral components of human bones and teeth [1–4]. HA is considered as an important bioactive and bioresorbable biomaterial widely used for bone tissue engineering, bone filling and substitution applications in orthopedics and dentistry [5–8]. Since the concept of biological surface science was established [9–11], the surface of biomaterials has been recognized to play a significant biological role, being the location of interaction with host biological media. Indeed, the analysis of various failed implants in the last decades indicated that failure mainly originates at the tissue/biomaterial interface [12]. Hence, a deep understanding of the biomaterial surface characteristics, in particular to elucidate the relationship between the types of surface terminations and the fate of the interactions with biomolecules, is mandatory to attain an increasingly higher level of control over biomaterials-host tissue interactions. The role of surfaces is further amplified in the case of nanobiomaterials; among them is nanosized hydroxyapatite, mimicking apatite nanocrystals in natural bone and teeth [13]. For instance, nanosizing and hierarchical structuring down to nanoscale of synthetic hydroxyapatite was found to have a beneficial effect on the response elicited in osteoblasts [14–16]. HA nanoparticles (NPs) can easily be prepared with different morphologies, namely needle-like [17–20] or plate-like [21,22]. Their surface/interface properties have been studied with a large variety of techniques (HR-TEM, MIR, NIR, NMR, ζ-potential) [23–26], combined with computational studies [27–29], allowing a precise knowledge of the atomic distribution of the exposed surfaces. Focusing on the types of surface facets, recent advances resulting from XRD [30] and HR-TEM investigations [31,32] indicated that, independently on the hexagonal or platelet morphology, the prevailing surfaces are often of the $\{01\bar{1}0\}$ type, corresponding to both lateral facets of hexagonal HA nanoparticles and basal facets

of platelets. Noticeably, $\{01\bar{1}0\}$ surfaces are considered good models of the prevailing facets exposed by nanoapatite crystals in bone [33]. However, it is known that $\{01\bar{1}0\}$ can exhibit different terminations depending on the specific interruption of the …-A-B-A-A-B-A-A-B-A-… sequence along the axis normal to the $\{01\bar{1}0\}$ crystal plane family, where A and B correspond to layers with $Ca_3(PO_4)_2$ and $Ca_4(PO_4)_2(OH)_2$ composition, respectively. As a consequence, three different types of $\{01\bar{1}0\}$ terminations are possible, indicated as stoichiometric HA $\{01\bar{1}0\}$ (upmost three layers: ...-A-B-A), HA $\{01\bar{1}0\}$_Ca-rich (upmost three layers: …-A-A-B) and HA $\{01\bar{1}0\}$_P-rich (upmost three layers: …-B-A-A). The labels Ca-rich and P-rich stem from a Ca/P ratio higher and lower than bulk Ca/P ratio of 1.67, respectively [28].

Refinement of synthetic procedures resulting in micro- and nanoHA particles with defined shape and size [22], have led to studies on the adsorption of amino acids [34–36], peptides [35,37], proteins [38–40], and DNA [41,42], aimed at understanding complex biomolecule adsorption phenomena [43]. Indeed, adsorption depends on a number of parameters related to the incubation conditions (i.e. temperature [44], pH and ionic strength [45], buffering agent [46]), the biomolecule(s) (i.e. charge size and structural rigidity [47,48], as well as cooperative behavior of proteins [49]) and textural and structural features of the adsorbing surfaces. Focusing on this latter aspect, Lin et al. provided evidence of the beneficial effect of surface nanotexture of HA bioceramics on the adsorption of specific plasma proteins [15]. As far as the surface texture, in terms of crystallographic facets exposed, the Kandori group investigated extensively the different behavior towards protein adsorption of $\{0001\}$ surfaces with respect to$\{01\bar{1}0\}$. They were found to preferentially adsorb basic (e.g. lysozyme) and acid (e.g. BSA) proteins, respectively.[50–52] However, the recent awareness of the possible presence of different types of $\{01\bar{1}0\}$ terminations raises the question about any specific behavior towards protein adsorption. Indeed, differences in

the adsorption on $\{01\bar{1}0\}$_Ca-rich and $\{01\bar{1}0\}$_P-rich terminations of other types of biomacromolecules, namely DNA, were revealed by a combined experimental and computational study [42]. Similar observations were made in the case of the computational investigation of HA surfaces with the simple amino acid glycine [53].

Here we report the results of an experimental study of the adsorption of bovine serum albumin (BSA), widely used to investigate the interaction of nanobiomaterials with proteins, on two nanoapatites, both preferentially exposing $\{01\bar{1}0\}$ surfaces (by high resolution transmission electron microscopy, HR-TEM) but with significantly different Ca-rich/P-rich terminations. The relative amount of these terminations was determined by analyzing IR spectra of adsorbed CO using the method developed in ref [54]. Aspects dealing with protein coverage were analyzed, taking into consideration the agglomeration state of apatite nanoparticles in the incubation experiments. Finally, the impact of the different Ca-rich/P-rich terminations ratio on the secondary structure of adsorbed proteins was determined by circular dichroism-UV spectroscopy (CD-UV).

EXPERIMENTAL SECTION

Materials. All solvents and reagents [calcium hydroxide $Ca(OH)_2$, phosphoric acid H_3PO_4, magnesium chloride hexahydrate $MgCl_2 \cdot 6H_2O$, ammonia, HEPES buffer, BSA] were high-purity Sigma-Aldrich products and used as received. MilliQ water was used throughout. High-purity CO (Praxair) was used for IR measurements without any additional purification, except liquid nitrogen trapping.

Preparation of HA NPs. In order to prepare 0.01 mol of hydroxyapatite, 0.10 mol of calcium hydroxide and 0.06 mol of phosphoric acid were combined. Calcium hydroxide was stirred magnetically in 200 ml of MilliQ water for 20 min until a homogeneous suspension was obtained. Phosphoric acid (diluted with 200 ml of MilliQ water) was added dropwise to this suspension over 45 min, with continuous stirring, keeping the pH above 10.5 by addition of ammonia solution, as necessary. The solution was stirred for a further 2 h, and then left overnight. The product was filtered under suction and dried at ambient conditions. For HA-LT (LT = low temperature) all the synthesis steps were carried out at 298 K, while for HA-HT (HT = high temperature) the temperature was kept at 368 K.

High Resolution Transmission Electron Microscopy (HR-TEM). HR-TEM images were obtained with a 3010 Jeol instrument operated at 300 kV. Samples were prepared by spreading a droplet of an aqueous suspension of nanoparticles on a copper grid coated with a lacey carbon film and then waiting for liquid evaporation. As apatite samples might evolve under the electron beam, potentially leading to further crystallization and/or loss of bulk water [55–57], TEM analysis was carried out under low-illumination conditions to avoid significant modification to the materials.

X-ray Diffraction (XRD). XRD patterns of HA powders were recorded with an Analytical X'Pert Pro equipped with a PIXcel detector powder diffractometer using Cu Kα radiation

(k = 1.5418 Å) generated at 45 kV and 40 mA. For the diffracted beam an automatic-variable anti-scatter slit with an irradiated length of 10 mm was used. The 2θ range was from 5° to 80° with a step size (2θ) of 0.039 and a counting time of 3 s.

Specific Surface Area (SSA_{BET}) Measurements. Specific surface areas of HA nanoparticles were measured by N_2 adsorption–desorption isotherms at 77 K using a Micromeritics ASAP 2020 instrument and SSA was calculated by the Brunauer–Emmett–Teller (BET) method.

IR Measurements. Infrared measurements were performed on powders pressed in self-supporting pellets and placed in a cell, equipped with KBr windows, allowing the collection of spectra at *ca.* 100 K (by liquid N_2 cooling). The cell was connected to a conventional vacuum line (residual pressure = 1×10^{-5} mbar, 1 mbar = 100 Pa) to perform all thermal treatments and adsorption-desorption experiments in situ. The spectra were collected at a resolution of 4 cm^{-1} with a Bruker IFS28 spectrometer, equipped with a DTGS detector. Each set of measurements (150 scans) was carried out on three different samples of each material, and data were normalized with respect to both the SSA for a comparative analysis and to the intensity of a pattern in the 2200-1900 cm^{-1} range (due to a combination and overtone of vibrational modes of bulk phosphate groups) to render differences in intensity independent of differences in the thickness of the pellets. Spectra of adsorbed CO are reported in Absorbance, after subtraction of the spectra of the sample before CO admission. The IR spectra at the highest CO coverage were analyzed in terms of linear combination of the theoretical spectra of $(CO)_n$-Ca^{2+} adducts ($4\geq n\geq 1$) calculated for CO on different HA surface terminations (from ref. [54], see Figure S1 in the Supporting Information, hereafter SI). In summary, for each structure *i* of carbonyl adducts (containing from 1 to 4 CO molecules) computed in ref. [54], the CO stretching IR spectrum $S_i(\nu)$ was computed as a linear combination of Gaussian functions $G(\nu - \nu_j)$, each one centered at the *j*th CO B3LYP rescaled

frequency value ν_j, and a 15 cm^{-1} full width at half-maximum (FWHM), weighted by the corresponding calculated IR intensity (I_j)

$S_i(\nu) = \Sigma I_j \, G(\nu - \nu_j)$

Hence, at this level, the only guess was the FWHM value adopted, which was consistent with the FWHM = 15 cm^{-1} of the νCO band at very low CO coverage, where only monocarbonyls, producing a single band, should be overwhelmingly present.

A linear combination $T(\nu)$ of all the computed $S_i(\nu)$ spectra represents the resulting spectrum in which, however, the weights w_i of each $S_i(\nu)$ have to be, somehow, determined

$T(\nu) = \Sigma w_j \, S_i(\nu)$

The criterion adopted to choose the weights w_i has been to run a nonlinear regression between the experimental IR spectrum and the computed $T(\nu)$ one, by keeping constant the relative ratios of the computed I_j intensities within the same case *i*, while changing their absolute values.

Dynamic Light Scattering (DLS). For DLS measurements a 90Plus Particle Size Analyzer (Brookhaven Instruments) was used (laser wavelength 663 nm, detection angle 90°, temperature 293 K). HA NPs were suspended (0.5 $mg \cdot ml^{-1}$) in bare HEPES (pH 7.4) and in BSA solutions buffered with HEPES. Moreover, DLS measurements were also performed on HA NPs carrying proteins irreversibly adsorbed toward dilution (namely protein hard corona, hereafter referred to "irreversibly adsorbed proteins"), separated by centrifugation from the BSA incubation solutions and resuspended in bare HEPES (see "Adsorption of BSA on HA samples" section for the detailed procedure). HEPES and buffered BSA solutions were the relevant media for this study, but in order to attain the highest dispersion of HA NPs, samples were also suspended in 0.1 M sodium citrate solution and stirred at 348 K for 24 h, to properly evaluate the NPs agglomeration occurring in other media. Moreover, DLS data of BSA solutions were acquired, for the sake of comparison.

For each suspension condition, DLS measurements were performed in triplicate and results reported as mean values of hydrodynamic diameters (Dh) ± standard deviation.

ζ-potential. The ζ–potential of samples (BSA in buffer, nanoparticles in the relevant dispersion media and NPs carrying the irreversible fraction of adsorbed proteins) was measured by electrophoretic light scattering (ELS) with a Zetasizer Nano-ZS (Malvern Instruments). Data are reported for each sample as mean values of triplicate experiments.

Adsorption of BSA on HA Samples. For both types of HA, a series of 6 suspensions, repeated in triplicate, were prepared (25 mg of powder in 2.5 ml of HEPES) and sonicated for 15 min at 298 K. An equal volume of BSA solution in HEPES were added for each sample obtaining, in a final volume of 5 ml, a series of incubation solutions with different initial protein concentration: 0.1, 0.5, 1.0, 2.5, 5, and 7.5 $mg \cdot ml^{-1}$. Samples rotated end-over-end for 15 min at 298 K, were then centrifuged for 20 min (10000 rpm, 298 K) to separate powders from the incubation media. Incubation times long up to 1 h were tested, but no significant changes in amount of adsorbed proteins and DLS values were obtained (Figure S2 in the SI). In order to desorb toward dilution the fraction of reversibly adsorbed BSA, pellets underwent several re-suspension/centrifugation cycles with fresh buffer and were then re-suspended in 5.0 ml of HEPES for spectrophotometric analyses.

Quantification of Adsorbed BSA. Adsorption curves of BSA on HA NPs were obtained by spectrophotometric measurement of the difference in the absorbance value at λ = 280 nm (Cary 300 Bio, Varian) to evaluate the protein concentration before and after contact with the powders. The specific aim was to obtain quantitative information on both the reversibly and irreversibly adsorbed protein components. The supernatants resulting from the first centrifugation after incubation of HA NPs in the BSA buffered solutions were analyzed spectrophotometrically,

to determine the concentration/amount of proteins remained in solution. These values were used for plotting relevant physical-chemical parameters as a function of the actual concentration of BSA in solution in equilibrium with the adsorbed one. The amount of BSA in solution was subtracted from the initial amount of proteins before contacting NPs in the incubation systems, thus resulting in the total (reversible + irreversible) amount of adsorbed proteins. Finally, for each sample, the supernatants obtained by the subsequent washing procedure (re-suspension/centrifugation cycles) were merged and the absorbance at 280 nm was measured in order to estimate the amount of reversibly adsorbed proteins. These values, subtracted from the total amount, gave the amount of irreversibly adsorbed proteins. Results are reported as the mean value of at least three separate experiments ± standard deviation.

Circular Dichroism Spectroscopy (CD-UV). A solution of 0.1 $mg \cdot ml^{-1}$ of BSA in MilliQ water (HEPES buffer is not transparent in the range of 180–210 nm for CD measurements) was prepared, and an aliquot was heated for 15 min at 373 K (with PTC-423S Peltier heating/cooling system in a tapped cuvette to prevent evaporation). Both solutions were scanned in the far-UV spectral range (180-300 nm, 4 accumulations, path length 0.1 cm, bandwidth 1 nm, scanning speed of 50 $nm \cdot min^{-1}$) using a Jasco J-815 spectropolarimeter equipped with a Xe arc lamp. Samples of HA NPs carrying the irreversible fraction of adsorbed BSA were suspended in MilliQ water and diluted in order to minimize the scattering due to particle suspension, attaining a final powder concentration of 0.5 $mg \cdot ml^{-1}$ just before acquiring spectra. BSA concentration in each suspension was then determined and adjusted to obtain the same nominal concentration of irreversibly adsorbed BSA per volume (see details in the SI). Deconvolution of CD spectra was performed with CDNN software (Version 2.1, Copyright (C) 1997 Gerald Böhm) to estimate the relative percentage of secondary structures, considering the maximum number (33) of reference spectra in the software

database. The effectiveness of this deconvolution method was confirmed also by the agreement of results obtained for native and thermally treated BSA in solution with literature data.

RESULTS AND DISCUSSION

Structure, Morphology and Size of HA NPs. Both HA-HT and HA-LT, exhibited XRD patterns (Figure S3) typical of single phase hexagonal hydroxyapatite (JCPDS 9-432).

In HR-TEM images (Figure 1), heavily affected by a tight agglomeration of nanoparticles on the support, both HA-HT (panel A) and HA-LT (panel B) in most cases produced elongated 2D projections on the image plane, with a different contrast (of the mass-thickness type) dependent on their width (normal to the elongation direction): narrower the width, higher the contrast (darker the particle image). This suggest that nanoparticles might exhibit an elongated plate-like shape, with size (length × width × thickness) of *ca.* 150-100 nm × 40-20 nm × 5-10 nm. Such dimensions are in agreement with a SSA_{BET} of 76 and 73 $m^2 \cdot g^{-1}$ measured for HA-HT and HA-LT, respectively. For nanoparticles properly oriented with respect to the electron beam lattice fringes due to $\{01\bar{1}0\}$ planes of hexagonal hydroxyapatite phase appeared. It was noted that these fringes run along the main side of the projection of NPs on the image plane indicating that both HA-HT and HA-LT nanoparticles are elongated along the *c*-axis. Moreover, the main borders of the nanoparticle projection appeared parallel to the lattice fringes, indicating that they correspond to the lateral view of $\{01\bar{1}0\}$ facets.

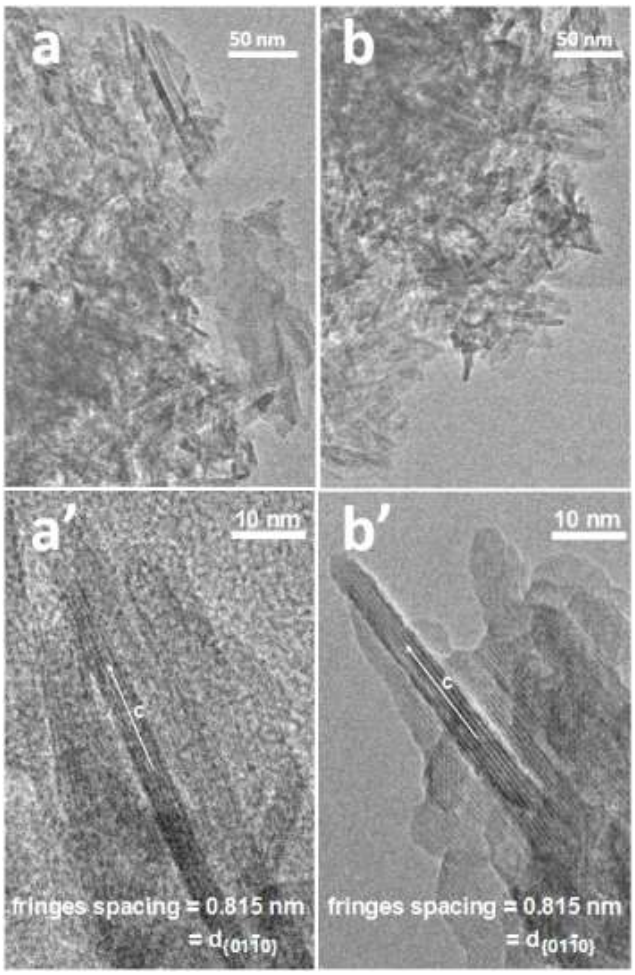

Figure 1. Representative HR-TEM images of HA-HT (panels (a), (a')), HA-LT (panels (b), (b')).Original magnifications: (a), (b) 35k ×; (a'), (b') 200k ×.

Types of HA Surface Terminations. The information provided by HR-TEM can be limited from a statistical point of view, and the sensitivity of HA nanoparticles to the exposure to the electron beam can prevent in a large extent the possibility to image details useful for the recognition the structure of surfaces. Thus, a method based on the analysis of the IR spectra of adsorbed CO was used to obtain insights on the relative amount of the different types of surface terminations exposed by HA nanoparticles [32,54]. In each of these measurements, milligrams of material are analyzed, instead of some hundreds of nanoparticles inspected by TEM, and the

experimental conditions adopted allow CO molecules to probe the local structure of all Ca^{2+} ions exposed to the surfaces of nanoparticles. Figure S4 shows the IR spectra of CO dosed on HA-HT and HA-LT (panels A and B, respectively) in order to saturate their capacity toward the adsorption of probe molecules on surface Ca^{2+} sites. The whole series of spectra collected at decreasing CO for both HA samples is reported in Figure S5 in the SI. The spectra at saturated CO coverage were compared with the unbiased sum (black dotted spectrum) of theoretical spectra (Sx curves, $4 \geq x \geq 1$), each with weight=1, due to all possible Ca^{2+}-$(CO)_n$ adducts ($4 \geq n \geq 1$) calculated for carbon monoxide on {0001}, stoichiometric $\{01\bar{1}0\}$ reacted (R) with water, $\{01\bar{1}0\}$_Ca-rich and $\{01\bar{1}0\}$_P-rich surface terminations [54]. The huge misfit clearly indicated that only some of the carbonylic adducts might have been formed on the surface of the two HA samples. A nonlinear regression between the computed sum and the experimental IR spectra was then run. In both cases the best fit resulted from the combination of components due only to carbonylic adducts on $\{01\bar{1}0\}$_Ca-rich and $\{01\bar{1}0\}$_P-rich surfaces, whereas the coefficient of all other theoretical spectra approached a value close to zero, indicating that the other types of surfaces contribute in a very minor extent to nanoparticle terminations. Noteworthy, the relative amount of $\{01\bar{1}0\}$_Ca-rich and $\{01\bar{1}0\}$_P-rich terminations appeared reversed in the two samples: *ca*. 2:1 for HA-HT and *ca*. 1:2 for HA-LT (Table 1). These reversed ratios are also in agreement with the results of ζ-potential measurements, i.e. of the assessment of the average surface charge of the two nanoparticle samples. On the basis of the findings of del Valle et al. [42], a larger relative amount of $\{01\bar{1}0\}$_Ca-rich terminations, which expose Ca^{2+}, OH^- and PO_4^{3-} is consistent with the more negative ζ-potential measured for HA-HT (-16.7 mV) than for HA-HT (-12.3 mV), where $\{01\bar{1}0\}$_P-rich terminations should be the more abundant.

Table 1. Table 1. $\{01\bar{1}0\}$_Ca-rich: $\{01\bar{1}0\}$_P-rich ratio of HA-HT and HA-LT

Material	$\{01\bar{1}0\}$_Ca-rich : $\{01\bar{1}0\}$_P-rich
HA-HT	2.00±0.06 : 1.00±0.04
HA-LT	1.00±0.05 : 2.20±0.06

Agglomeration Status and ζ–potential of HA-NPs in BSA Solutions. The hydrodynamic diameter (Dh) of HA NPs suspended in HEPES buffer in their bare form and carrying irreversibly adsorbed proteins was measured by DLS. Mass distribution data resulting from the average of 3 measurements are reported in Figure 2, panel A. The whole set of raw data of BSA in HEPES and of HA NPs in the various suspension conditions considered are reported in Figure S6 and S7, respectively, in the SI.

The highest dispersion of HA NPs was pursued and best results were found by using a citric acid solution with pH adjusted to 6.5 by NaOH addition. In this condition, HA-HT exhibited a bimodal distribution with Dh values of *ca.* 100 and 400 nm (panel A, black dashed lines a, a', respectively; ratio in mass 1:2, see Figure S7 in the SI), whilst for HA-LT the distribution appeared monomodal, with an average Dh of *ca.* 380 nm (panel A, green dashed line b). The Dh value around 100 nm found for HA-HT, is similar to the size of primary particles observed by HR-TEM, indicating that the suspension medium used allows a monodispersion of the nanoparticles. Consequently, the Dh values around 380/400 nm indicated that *ca.* 2/3 of HA-HT and the whole HA-LT sample are constituted by aggregates of multiple nanoparticles.

Hence, the citric acid solution appeared a good suspension medium for attaining a high dispersion of HA nanoparticles. This behavior likely resulted from the adsorption of citrate anions, that were reported to strongly interact with the surface of apatite nanocrystals [30,33]. As a

consequence, this medium was not considered for studying the adsorption of BSA, in order to avoid the interference of citrate ions in this phenomenon.

When suspended in HEPES buffer, both single and aggregated NPs of HA-HT underwent a large agglomeration, as indicated by the appearance of a monomodal distribution with an average Dh of *ca.* 1.6 µm. In the case of HA-LT the agglomeration was so extended to result in the flocculation of the system (amount of agglomerates remained in suspension too low to produce a detectable signal in DLS measurements).

HEPES buffered solutions of BSA were then added to HA-LT and HA-HT suspended in HEPES buffer. Dh was measured in two conditions, and equivalent results were obtained: i) with unadsorbed proteins still present in the suspension (thus before any centrifugation), ii) after removing them, by separating NPs with irreversibly adsorbed BSA and re-suspending them in HEPES buffer (see Figure S8 in the SI). The second condition was also used for the ζ–potential measurements, to avoid contribution from non-adsorbed proteins.

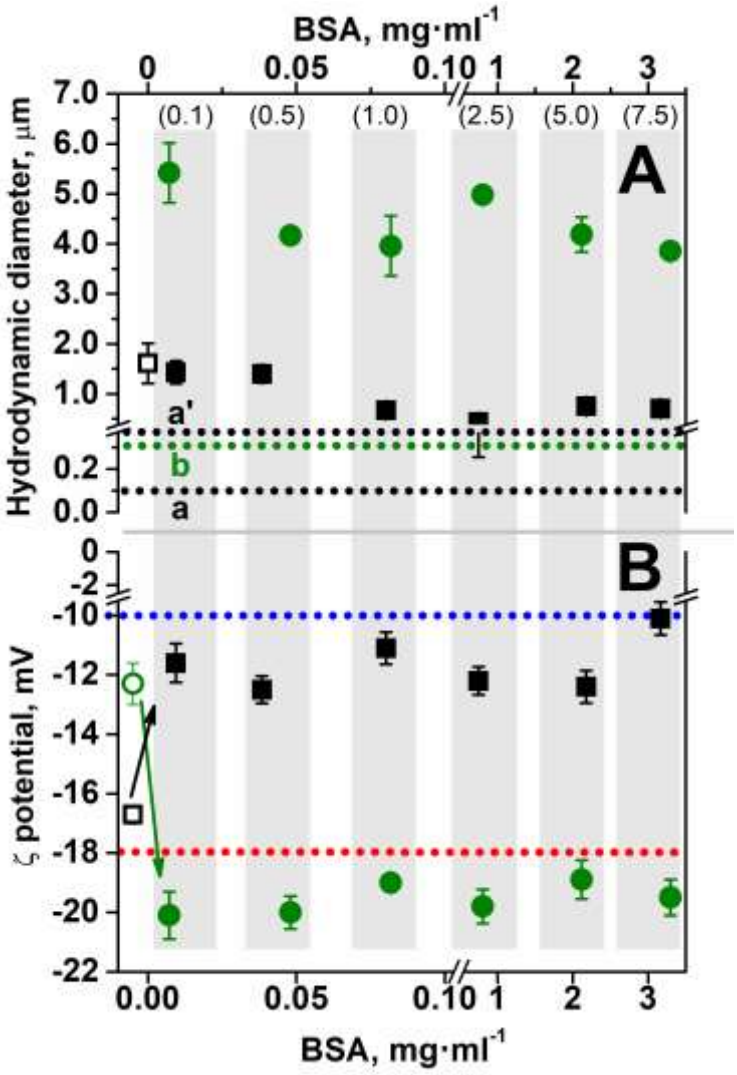

Figure 2. Panel (a): hydrodynamic diameter (Dh) of HA-HT (color code: black), HA-LT (color code: green) suspended in: (i) solution of sodium citrate 0.1M ((a), (a') and (b) dotted lines), (ii) HEPES buffer (HA-HT: empty symbols; HA-LT: agglomerates too large in size to be measured) and (iii) re-suspended in HEPES after incubation with BSA solution with different concentrations (full symbols) and removal of BSA adsorbed reversibly upon dilution (see Experimental). Panel (b): ζ-potential of: (i) native and thermally treated BSA in solution (blue and red dotted lines, respectively) and (ii) HA-HT and HA-LT NPs in bare form (empty symbols) and with irreversibly adsorbed BSA (full symbols), as in panel (a) (again, values reported on the X-axis: concentration of BSA in solution in equilibrium with the adsorbed one). Values reported on the X-axis: concentration of BSA in solution in equilibrium with the adsorbed one, at the end of the incubation. Values in brackets over grey bars are initial concentrations of BSA solutions.

An overall dispersive effect of BSA molecules was observed. In the case of HA-HT, a slight decrease of Dh occurred for NPs incubated in 0.1 and 0.5 $mg \cdot ml^{-1}$ protein solutions, whilst Dh more than halved for incubation in more concentrated BSA solutions. In any case, a dispersion as high as in the citrate solution was not attained. Protein molecules also acted as dispersing agents toward HA-LT agglomerates, which however, remained very large in size, from *ca.* 5.5 to 4 μm.

The dispersive effect of proteins toward agglomeration of both types of HA NPs appeared qualitatively similar to observations in a previous work for silica nanoparticles [58]. This behavior was interpreted in terms of diffusion of protein molecules within interparticle spaces in the initial agglomerates, which are then partly disrupted.

The incomplete redispersion indicates that the diffusion process did not reach the core of agglomerates. Consequently, DLS is actually measuring the size of the fragments of agglomerates that resisted the diffusion of BSA molecules, carrying adsorbed proteins on the surface accessible to BSA molecules.

Complementary aspects of the HA NPs-BSA interaction were studied by measuring the ζ–potential of HA-HT and HA-LT suspended in HEPES buffer in their bare form or when carrying on their surface the hard protein corona. Data are shown in Figure 2, panel B, where also the ζ–potential values of BSA in HEPES buffer in the native state (blue dotted line) and after thermal treatment (red dotted line) are reported for the sake of comparison.

As reported above, ζ–potential values measured for bare HA-HT and HA-LT were −16.7 and −12.3 mV, respectively. Noticeably, an opposite evolution of ζ–potential occurred as a consequence of the presence of irreversibly adsorbed proteins: by incubation with the less concentrated BSA HEPES buffered solution (0.1 $mg \cdot ml^{-1}$), the ζ–potential measured for HA-HT increased from −16.7 mV to −12.1 mV ($\Delta\zeta$= +4.6 mV), whereas for HA-LT it decreased from

−12.3 mV to −20.1 mV (Δζ= -7.8 mV). By incubation with more concentrated BSA solutions, up to an equilibrium concentration of ca. 3.0 mg·ml^{-1} (initial BSA concentration 7.5 mg·ml^{-1}), ζ–potential changed in a more limited way, remaining in the -12.0/−10.0 mV range for HA-HT, and −20.1/−18.0 mV range for HA-LT. Noteworthy, the ζ–potential values of the BSA on HA-HT system and of the BSA on HA-LT one are similar to those of native and thermally treated BSA in solution, respectively (dotted lines in Figure 2B).

Such opposite behavior clearly indicated that the adsorption of BSA molecules is significantly influenced by the different $\{01\bar{1}0\}$_Ca-rich:$\{01\bar{1}0\}$_P-rich terminations ratio between the two HA samples. The ζ–potential of a protein-on-NPs system depends on both protein coverage and structure. Thus, these aspects were also investigated.

Amount of Adsorbed BSA and Surface Coverage. Total and irreversibly adsorbed amounts of BSA per unit mass of the two materials, with dependence on the initial concentration of the protein incubation solutions, are shown in Figure 3A. For each type of HA NPs, the two sets of data appeared almost coincident, indicating that the overwhelming part of BSA adsorption had an irreversible character. Nevertheless, in no case a complete adsorption of BSA present in the incubation medium occurred. Thus, for the sake of simplicity, only data dealing with the irreversibly adsorbed amounts were further considered.

The next step was the evaluation of the surface coverage, assuming a BSA molecule should occupy an area of ca. 9.0 × 5.5 nm^2 when adsorbed in a “side-on” manner (a conservative choice with respect to the “end-on” mode, resulting in the occupation of a smaller 5.5 × 5.5 nm^2 area) [59]. As far as the surface area of HA NPs for protein adsorption is considered, the SSA_{BET} values (then measured by N_2 adsorption on dry powders) were used, and the results obtained are reported in Figure 3, panel B, in terms of relative coverage with respect to a theoretical monolayer of

"side–on" adsorbed BSA molecules. The data sets appeared quite similar for both HA-HT and HA-LT, exhibiting a progressive increase of the coverage up to 0.6 for BSA initial concentration as large as 1.0 $mg \cdot ml^{-1}$, and then exhibiting oscillations in the 0.4-0.7 θ value range for higher BSA initial concentrations.

Noteworthy, the incubation with BSA solutions at different initial concentrations up to 1 mg/ml resulted in a different dispersion of HA NPs agglomerates (Figure 2, panel A). Thus, it must be considered that each of the three first points in the adsorption isotherms in Figure 3 results from an incubation condition where two parameters are different with respect to the other points: not only the initial/equilibrium protein concentration, but also the size of the HA NPs agglomerates, i.e. the amount of surface area available for protein adsorption. Hence, the linear trend of the initial part of the isotherms cannot be interpreted on the basis of the usual models developed for the protein adsorptions on substrates not changing in size in dependence on the protein concentration.

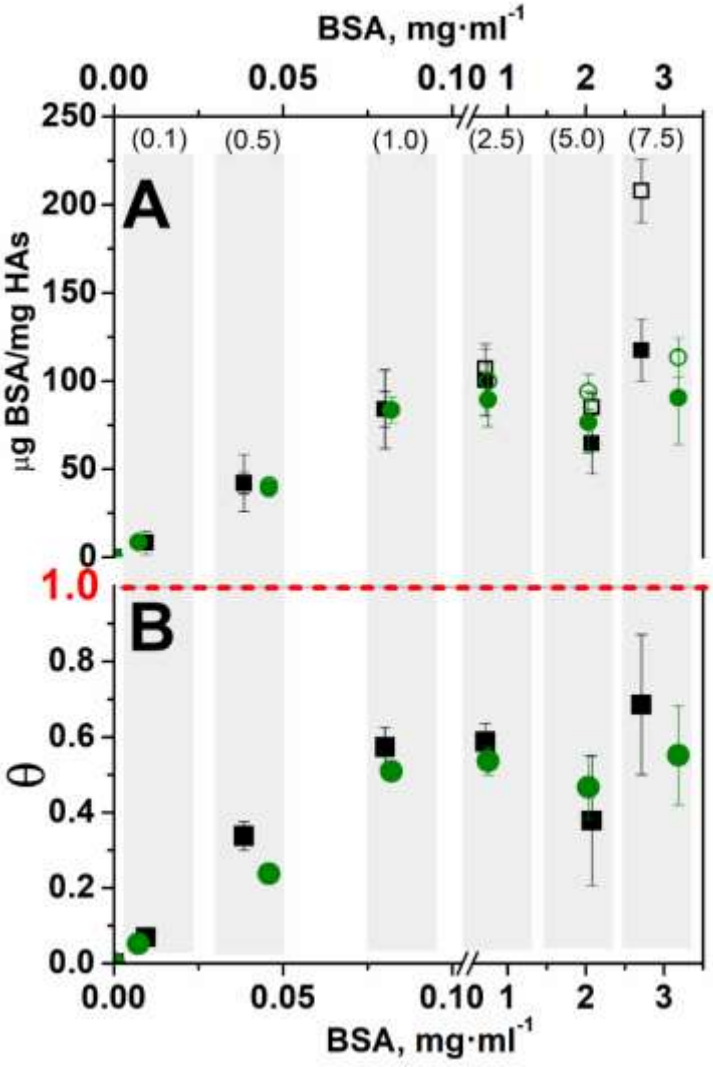

Figure 3. Panel (a): amount of total (empty symbols) and irreversibly (full symbols) adsorbed BSA on HA-HT (black squares) and HA-LT (green circles) after incubation in different BSA solutions with different protein concentrations reported per mass of HA powder. Evaluation of HA surface coverage by irreversibly adsorbed BSA by considering: panel (b) the SSA measured by the BET method. Red dashed line, $\theta = 1$: theoretical monolayer, for BSA adsorption in the side-on mode [59]. Values reported on the X-axis: concentration of BSA in solution in equilibrium with the adsorbed one, at the end of the incubation. Values in brackets over grey bars are initial concentrations of BSA solutions.

However, it must be considered that an extensive agglomeration of both types of HA nanoparticles occurred in HEPES buffer, and that the partial redispersion attained when BSA was added witness for the limited diffusion of proteins within the agglomerates. Thus, the surface per unit of mass of HA actually available for the adsorption of BSA molecules should have been significantly lower with respect the SSA_{BET}. As a consequence, in both HA-HT and HA-LT agglomerated the protein coverage should be higher than what reported in Figure 3, panel B. In a previous study dealing with adsorption of BSA on spherical SiO_2 NPs [58], the high homogeneity in shape and size of nanoparticles resulted in the agglomeration of nanoparticles in a hexagonal array, and this allowed for a reasonable estimation of the mass present in the agglomerates and of their external surface area, accessible to BSA molecules. The different shape of HA nanoparticles and the unknow shape and structure of agglomerates prevented a similar analysis in the present case. Nevertheless, it must be considered that the ζ–potential of a protein-NP system results from the combined contribution adsorbed proteins and the part of the surface of nanoparticles still uncoated by them. Thus, the dependence of ζ–potential and of surface coverage from the protein concentration in the incubation suspensions should be similar, whereas this was not the case for BSA on HA-HT and HA-LT. The trend of protein coverage calculated on the basis of the SSA_{BET} was characterized by an almost linear increase by increasing up to 1.0 $mg \cdot ml^{-1}$ the BSA concentration of the incubations solutions (Figure 3, panel B). Conversely, a steep change of ζ–potential occurred when passing from bare nanoparticles to the presence of irreversibly adsorbed protein by contact with a 0.1 $mg \cdot ml^{-1}$ BSA solution, and then more limited changes occurred for proteins-NPs systems resulting from the suspension in more concentrated BSA solutions (Figure 2, panel B). This behavior suggests that, for each type of HA material, the extent of the surface of agglomerated nanoparticles coated by irreversibly adsorbed proteins should have been almost

constant along the series of protein-NPs systems resulting from incubations in BSA solutions with different protein concentration.

Confirmatory evidence of these proposals was obtained by CD-UV spectroscopy, also providing insights on the conformation of adsorbed proteins.

CD-UV of BSA Irreversibly Adsorbed on HA. CD–UV spectra of proteins irreversibly adsorbed on HA-HT and HA-LT (curves a-d and a'-d', respectively) are reported in Figure 4. In order to properly relate possible changes in the intensity of the CD-UV signals to structural modification due to adsorbed proteins, spectral intensities were normalized with respect to the same protein content (for details, see Figure S9 and related comment in the SI). Moreover, spectra of adsorbed proteins are compared with those of BSA in solution in both native and thermally treated forms (blue and red dashed curves, respectively). The latter was of interest as a case where protein underwent changes in the secondary structure, without aggregation.

The CD-UV spectrum of native BSA in solution exhibits the usual profile characterized by one positive signal at 192 nm and a negative partner at 208 nm (resulting from the exciton coupling splitting of the $\pi \rightarrow \pi^*$ transition) and a negative component at 222 nm due to the $n \rightarrow \pi^*$ transition [60,61]. Following thermal treatment, the total intensity of these signals decreased and also a change in their relative intensity occurred. Spectra were deconvoluted (CDNN software; results in Table 2) and the relative amount of α-helix, β-sheet and unordered secondary motifs found for native BSA appeared fully consistent with literature values [62].

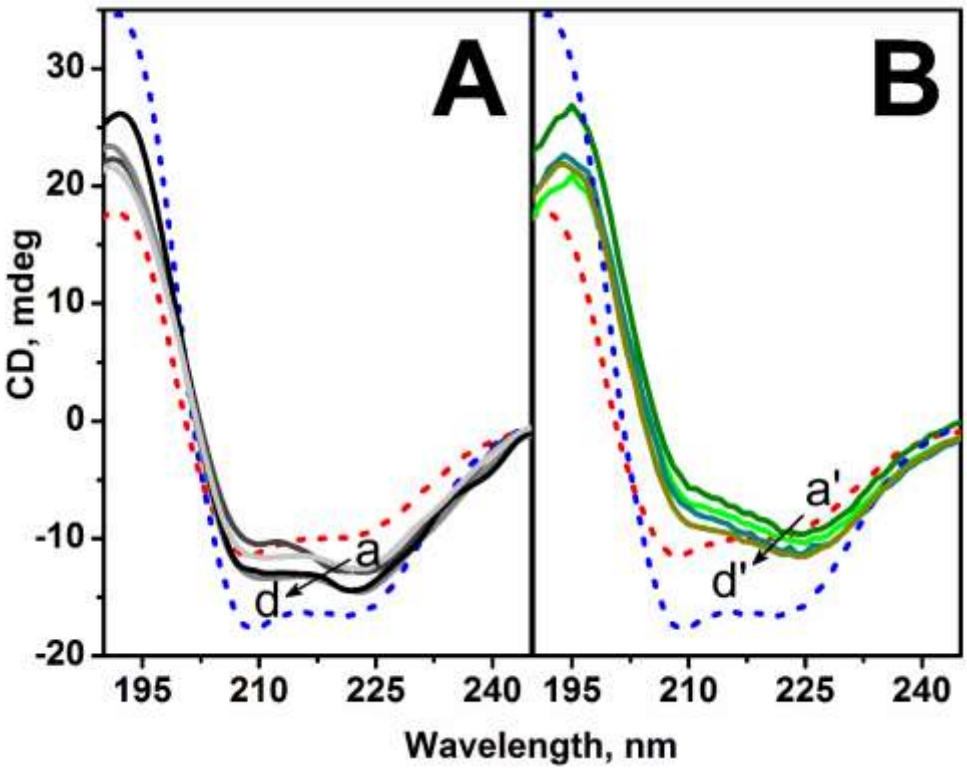

Figure 4. CD-UV spectra of BSA irreversibly adsorbed on HA-HT and HA-LT (panels (a) and (b), respectively) incubated in protein solutions at different initial concentration: (a),(a') 0.1, (b),(b') 0.5, (c),(c') 2.5, (d),(d') 7.5 mg ml^{-1}. Spectra are compared with those of BSA solutions in native form and after thermal treatment at 373 K for 15 min (blue and red dashed curves, respectively).

As expected, the relative amount of α-helices decreased in favor of random coils (and in a minor extent of β-turns) for thermally treated BSA, whereas the relative amount of β-sheets remained almost unchanged, indicating that aggregation among proteins, resulting in the formation of intermolecular β-sheets-like structure, did not occur.

Considering irreversibly adsorbed proteins, the spectra of BSA on HA-HT (panel A, curves a-d) appeared located between those of native and thermally treated BSA. Moreover, they are very similar to each other, independently on the concentration of BSA in the incubation solution. The main difference with respect to the spectra of BSA in solution was a change in the relative intensity

of minima at 208 and 222 nm. Such a change appeared even more evident for spectra of BSA irreversibly adsorbed on HA-LT, all located over the spectrum of thermally treated BSA (panel B, curves a'-d'). These spectral behaviors clearly indicated that important changes in the relative amount of secondary structural motifs occurred in adsorbed proteins. By spectral analysis, an increase in β-sheet content deconvolution (Table 2, column 4) was found for BSA adsorbed on HA-HT and HA-LT, almost doubled with respect to proteins in solution in both their native and thermally treated forms. This finding, accompanied by a significant decrease in the 208/222 nm intensity ratio (Table 3), monitors the formation of intermolecular β-sheets, as observed for BSA assembly resulting from the interaction with cationic lipids [63], or the adsorption of amyloid proteins on Teflon particles [64].

Table 2. Relative amount of secondary structures obtained by deconvolution of CD-UV spectra of BSA in solution (native and thermal treated forms) and irreversibly adsorbed on HA-HT and HA-LT incubated in protein solutions at different initial concentrations.

Sample (BSA)	BSA, $mg \cdot ml^{-1}$ (initial concentration)	α-helix (%)	β-sheet (%)	β-turn (%)	random coil (%)
solution	0.1	69 ± 3	9 ± 2	10 ± 1	12 ± 2
solution (373 K)	0.1	48 ± 2	10 ± 2	16 ± 1	27 ± 2
BSA on HA-HT	0.1	55 ± 3	18 ± 1	10 ± 1	17 ± 2
	0.5	63 ± 2	18 ± 1	8 ± 1	11 ± 1
	2.5	56 ± 3	17 ± 1	10 ± 1	17 ± 2
	7.5	59 ± 3	18 ± 1	10 ± 1	13 ± 1
BSA on HA-LT	0.1	40 ± 1	20 ± 1	11 ± 1	30 ± 1
	0.5	40 ± 2	21 ± 1	10 ± 1	27 ± 2
	2.5	38 ± 2	21 ± 1	10 ± 1	30 ± 1
	7.5	40 ± 2	21 ± 1	9 ± 1	28 ± 2

Table 3. Ratio between CD values at 208 and 222 nm (CD_{208}/CD_{222}) calculated for CD-UV spectra of BSA in solution and adsorbed on HA NPs.

$CD_{208}/CD_{222} > 1$		$CD_{208}/CD_{222} < 1$	
BSA in solution		adsorbed BSA	
native BSA	1.07	0.89, 0.87, 0.78, 0.88	panel A, spectra a-d
heated at 373 K	1.16	0.64, 0.59, 0.61, 0.68	panel B, spectra a'-d'

The occurrence of protein-protein interactions among BSA molecules adsorbed on HA-HT and HA-LT can then be inferred. This can account for the formation of at least a protein monolayer on the parts accessible to BSA of the surface of nanoparticles forming the agglomerates. This finding confirms that the sub-monolayer protein coverage calculated by taking into consideration the SSA_{BET} was underestimated (Figure 3, panel B): when HA nanoparticles are agglomerated, their specific surface area accessible to proteins is lower than that measured by N_2 adsorption on dry powders. The formation of at least a BSA monolayer, likely occurring for all the BSA concentrations considered, should result from the combined increase of the amount of proteins in solution and of the protein-induced partial disagglomeration of nanoparticles, with a consequent increase of the surface area available for protein adsorption.

Another important feature is constituted by the different content in random coils (Table 2, column 6) and α-helices (Table 2, column 3) between BSA adsorbed on HA-HT and HA-LT.

In the case of BSA on HA-HT, the random coil content (11-17%) changed in a limited extent with respect to native BSA in solution (12±2%), whereas it increased significantly for BSA on HA-LT (27-30%). Accordingly, the α-helix content of BSA on HA-LT (38-40%) decreased in a larger extent with respect to native BSA in solution (69±3%), than for BSA on HA-HT (55-63%). In addition, it must be considered that, in both cases, a part of the decrease in intensity of the spectroscopic features due to α-helices is due to the protein-protein interactions responsible for β-sheet-like signals. Because the protocol for protein adsorption on the two HA NPs types was the same, the difference in random coil content points to a role of the ratio between $\{01\bar{1}0\}$_Ca-rich and $\{01\bar{1}0\}$_P-rich surface terminations in determining possible intramolecular conformational changes of adsorbed proteins.

Changes in secondary structure detected by CD-UV for native and thermally treated BSA in

solution resulted in a change in the protein ζ–potential (Figure 2B). Hence, the different conformation of BSA adsorbed on HA-HT and HA-LT can be related to the different ζ–potential of the two protein-NPs systems (Figure 2B). CD-UV data indicated that at least a protein monolayer was attained for both systems even when the agglomerates of HA nanoparticles were contacted with the BSA solution with initial concentration of 0.1 $mg \cdot ml^{-1}$. Hence, the ζ–potential measured was mainly due only to the protein layer(s), without any significant contribution from the underlying HA surface. In the case of BSA on HA-HT, the protein adsorption did not result in a significant change in the relative amount of unordered secondary structure, and the increase in the relative amount of β-sheet-like motifs monitors the occurrence of protein-protein interactions. Thus it can be proposed that BSA on HA-HT basically maintained their native structure, and the parts of the polypeptidic chain exposed towards the exterior contribute to the measured ζ–potential. Conversely, CD-UV spectra indicated that conformational changes occurred for BSA adsorbed on HA-LT. Because also in this case, the surface of agglomerates of HA nanoparticles is completely covered by adsorbed proteins, the measured ζ–potential should result from the ionizable chemical groups exposed towards the exterior by protein molecules. Owing to the differences in secondary structure, the amount and nature of these groups can be different from those determining the ζ–potential of BSA on HA-HT.

CONCLUSIONS

The collection of the results presented above point at two principal insights, one relevant for the methodologies to be adopted for the investigation of the adsorption of proteins on nanomaterials, and the other for the sensitivity of protein adsorption to surface features of nanomaterials.

As far as the methodological aspect is concerned, our data indicate that an important aspect of

the protein adsorption on nanoparticles, such as the protein surface coverage, cannot be determined taking into consideration the specific surface area of nanoparticles as measured by N_2 adsorption on dry powders (the so-called BET method). Conversely, it must be considered that nanoparticles can agglomerate in the incubation medium, thus the surface available for the adsorption of proteins is only that of nanoparticles exposed at the surface of agglomerates.

Passing to the impact of the protein-nanoparticles interaction on the protein secondary structure, it can be concluded that even differences in the atomic arrangement of surface termination of the same crystallographic type affect the conformation of adsorbed proteins. This insight extends to proteins what found by del Valle et al. [42] when studying the interaction of DNA with nano-HA, and adds a step to the elucidation of the effect of hierarchical nanostructuring of HA bioceramics on protein adsorption [15].

ASSOCIATED CONTENT

Supporting Information: theoretical and experimental IR spectra of CO adsorbed on HA surfaces; adsorption isotherms and DLS data at increasing incubation time; raw DLS data; description of normalization method for the comparison between UV-CD spectra of BSA in solution and UV-CD spectra of BSA irreversibly adsorbed on HA nanoparticles.

AUTHOR INFORMATION

Corresponding Author:

*Pavlo Ivanchenko, e-mail: pavlo.ivanchenko@unito.it; telephone number: +39-0116707538;

Author Contributions: FC and PI contributed equally to this work. The manuscript was written through contributions of all authors. All authors have given approval to the final version of the

manuscript.

Funding Sources: project “Nanomaterials for sustainable leather products - NanoSusLeather” – CSTO165920.

ACKNOWLEDGMENT

This work has been supported by the CSP-UniTo project “Nanomaterials for sustainable leather products - NanoSusLeather” – CSTO165920. F.C acknowledges the University of Torino and its Department of Chemistry for supporting his post-doc position (code A03.128/2015/XVIII). E.R acknowledges Kemia Tau S.R.L for supporting her PhD.

REFERENCES

[1] S.J. Eppell, W. Tong, J. Lawrence Katz, L. Kuhn, M.J. Glimcher, Shape and size of isolated bone mineralites measured using atomic force microscopy, J. Orthop. Res. 19 (2001) 1027–1034. doi:10.1016/S0736-0266(01)00034-1.

[2] P. Fratzl, H.S. Gupta, E.P. Paschalis, P. Roschger, Structure and mechanical quality of the collagen–mineral nano-composite in bone, J. Mater. Chem. 14 (2004) 2115–2123. doi:10.1039/B402005G.

[3] M.J. Olszta, X. Cheng, S.S. Jee, R. Kumar, Y.Y. Kim, M.J. Kaufman, E.P. Douglas, L.B. Gower, Bone structure and formation: A new perspective, Mater. Sci. Eng. R Reports. 58 (2007) 77–116. doi:10.1016/j.mser.2007.05.001.

[4] R.A. Young, W.E. Brown, Structure of Biological Minerals, in: G.H. Nancollas (Ed.), Biol. Miner. Deminer. Rep. Dahlem Work. Biol. Miner. Deminer., Springer Berlin Heidelberg, Berlin, 1982: pp. 101–141.

[5] S. V. Dorozhkin, Calcium orthophosphates in nature, biology and medicine, Materials (Basel). 2 (2009) 399–498. doi:10.3390/ma2020399.

[6] F.H. Jones, Teeth and bones: Applications of surface science to dental materials and related biomaterials, Surf. Sci. Rep. 42 (2001) 75–205. doi:10.1016/S0167-5729(00)00011-X.

[7] H. Liu, T.J. Webster, Nanomedicine for implants: A review of studies and necessary experimental tools, Biomaterials. 28 (2007) 354–369. doi:10.1016/j.biomaterials.2006.08.049.

[8] N. Roveri, B. Palazzo, Hydroxyapatite Nanocrystals as Bone Tissue Substitute, in: Nanotechnologies Life Sci., Wiley-VCH Verlag GmbH & Co. KGaA, 2007.

[9] D.G. Castner, B.D. Ratner, Biomedical surface science: Foundations to frontiers, Surf. Sci. 500 (2002) 28–60. doi:10.1016/S0039-6028(01)01587-4.

[10] B. Kasemo, Biological surface science, Surf. Sci. 500 (2002) 656–677. doi:Pii S0039-6028(01)01809-XDoi 10.1016/S0039-6028(01)01809-X.

[11] M. Tirrell, E. Kokkoli, M. Biesalski, The role of surface science in bioengineered materials, Surf. Sci. 500 (2002) 61–83. doi:10.1016/S0039-6028(01)01548-5.

[12] W.B. Greene, L.S. Dias, R.E. Lindseth, M.A. Torch, Musculoskeletal problems in association with cloacal exstrophy., J. Bone Joint Surg. Am. 73 (1991) 551–60. doi:10.2106/00004623-199173040-00012.

[13] P. Wang, L. Zhao, J. Liu, M.D. Weir, X. Zhou, H.H.K. Xu, Bone tissue engineering via nanostructured calcium phosphate biomaterials and stem cells, Bone Res. 2 (2015) 14017. doi:10.1038/boneres.2014.17.

[14] S. V. Dorozhkin, Nanosized and nanocrystalline calcium orthophosphates, Acta Biomater. 6 (2010) 715–734. doi:10.1016/j.actbio.2009.10.031.

[15] K. Lin, L. Xia, J. Gan, Z. Zhang, H. Chen, X. Jiang, J. Chang, Tailoring the nanostructured surfaces of hydroxyapatite bioceramics to promote protein adsorption, osteoblast growth, and osteogenic differentiation, ACS Appl. Mater. Interfaces. 5 (2013) 8008–8017. doi:10.1021/am402089w.

[16] T.J. Webster, R.W. Siegel, R. Bizios, Osteoblast adhesion on nanophase ceramics, Biomaterials. 20 (1999) 1221–1227. doi:10.1016/S0142-9612(99)00020-4.

[17] Y. Deng, H. Wang, L. Zhang, Y. Li, S. Wei, In situ synthesis and in vitro biocompatibility of needle-like nano-hydroxyapatite in agar-gelatin co-hydrogel, Mater. Lett. 104 (2013) 8–12. doi:10.1016/j.matlet.2013.03.145.

[18] H. Ito, Y. Oaki, H. Imai, Selective Synthesis of Various Nanoscale Morphologies of

Hydroxyapatite via an Intermediate phase, Cryst. Growth Des. 8 (2008) 1055–1059. doi:10.1021/cg070443f.

[19] C. Shuai, P. Feng, Y. Nie, H. Hu, J. Liu, S. Peng, Nano-hydroxyapatite improves the properties of β-tricalcium phosphate bone scaffolds, Int. J. Appl. Ceram. Technol. 10 (2013) 1003–1013. doi:10.1111/j.1744-7402.2012.02840.x.

[20] X. Yao, H. Yao, G. Li, Y. Li, Biomimetic synthesis of needle-like nano-hydroxyapatite templated by double-hydrophilic block copolymer, J. Mater. Sci. 45 (2010) 1930–1936. doi:10.1007/s10853-009-4182-4.

[21] L. Bertinetti, A. Tampieri, E. Landi, C. Ducati, P.A. Midgley, S. Coluccia, G. Martra, Surface structure, hydration, and cationic sites of nanohydroxyapatite: UHR-TEM, IR, and microgravimetric studies, J. Phys. Chem. C. 111 (2007) 4027–4035. doi:Doi 10.1021/Jp066040s.

[22] M. Sadat-Shojai, M.T. Khorasani, E. Dinpanah-Khoshdargi, A. Jamshidi, Synthesis methods for nanosized hydroxyapatite with diverse structures, Acta Biomater. 9 (2013) 7591–7621. doi:10.1016/j.actbio.2013.04.012.

[23] M. Aizawa, A.E. Porter, S.M. Best, W. Bonfield, Ultrastructural observation of single-crystal apatite fibres, Biomaterials. 26 (2005) 3427–3433. doi:10.1016/j.biomaterials.2004.09.044.

[24] L. Bertinetti, C. Drouet, C. Combes, C. Rey, A. Tampieri, S. Coluccia, G. Martra, Surface characteristics of nanocrystalline apatites: Effect of Mg surface enrichment on morphology, surface hydration species, and cationic environments, Langmuir. 25 (2009) 5647–5654. doi:10.1021/la804230j.

[25] C. Jäger, T. Welzel, W. Meyer-Zaika, M. Epple, A solid-state NMR investigation of the structure of nanocrystalline hydroxyapatite, Magn. Reson. Chem. 44 (2006) 573–580. doi:10.1002/mrc.1774.

[26] M. Rouahi, E. Champion, O. Gallet, A. Jada, K. Anselme, Physico-chemical characteristics and protein adsorption potential of hydroxyapatite particles: Influence on in vitro biocompatibility of ceramics after sintering, Colloids Surfaces B Biointerfaces. 47 (2006) 10–19. doi:10.1016/j.colsurfb.2005.11.015.

[27] N. Almora-Barrios, K.F. Austen, N.H. De Leeuw, Density functional theory study of the binding of glycine, proline, and hydroxyproline to the hydroxyapatite (0001) and (0110)

surfaces, Langmuir. 25 (2009) 5018–5025. doi:10.1021/la803842g.

[28] R. Astala, M.J. Stottt, First-principles study of hydroxyapatite surfaces and water adsorption, Phys. Rev. B. 78 (2008) 075427. doi:Artn 075427 10.1103/Physrevb.78.075427.

[29] N.H. de Leeuw, Resisting the Onset of Hydroxyapatite Dissolution through the Incorporation of Fluoride, J. Phys. Chem. B. 6 (2004) 1809–1811. doi:10.1021/jp036784v.

[30] J.M. Delgado-Lopez, R. Frison, A. Cervellino, J. Gomez-Morales, A. Guagliardi, N. Masciocchi, Crystal Size, Morphology, and Growth Mechanism in Bio-Inspired Apatite Nanocrystals, Adv. Funct. Mater. 24 (2014) 1090–1099. doi:10.1002/adfm.201302075.

[31] C.A. Ospina, J. Terra, A.J. Ramirez, M. Farina, D.E. Ellis, A.M. Rossi, Experimental evidence and structural modeling of nonstoichiometric (010) surfaces coexisting in hydroxyapatite nano-crystals, Colloids Surfaces B Biointerfaces. 89 (2012) 15–22. doi:https://doi.org/10.1016/j.colsurfb.2011.08.016.

[32] Y. Sakhno, P. Ivanchenko, M. Iafisco, A. Tampieri, G. Martra, A step toward control of the surface structure of biomimetic hydroxyapatite nanoparticles: Effect of carboxylates on the {010} P-rich/Ca-rich facets ratio, J. Phys. Chem. C. 119 (2015) 5928–5937. doi:10.1021/jp510492m.

[33] Y.Y. Hu, A. Rawal, K. Schmidt-Rohr, Strongly bound citrate stabilizes the apatite nanocrystals in bone, Proc. Natl. Acad. Sci. U. S. A. 107 (2010) 22425–22429. doi:10.1073/pnas.1009219107.

[34] R. Goobes, G. Goobes, W.J. Shaw, G.P. Drobny, C.T. Campbell, P.S. Stayton, Thermodynamic roles of basic amino acids in statherin recognition of hydroxyapatite, Biochemistry. 46 (2007) 4725–4733. doi:10.1021/bi602345a.

[35] A. Rimola, M. Aschi, R. Orlando, P. Ugliengo, Does adsorption at hydroxyapatite surfaces induce peptide folding? Insights from large-scale B3LYP calculations, J. Am. Chem. Soc. 134 (2012) 10899–10910. doi:10.1021/ja302262y.

[36] A. Rimola, M. Corno, C.M. Zicovich-Wilson, P. Ugliengo, Ab initio modeling of protein/biomaterial interactions: Glycine adsorption at hydroxyapatite surfaces, J. Am. Chem. Soc. 130 (2008) 16181–16183. doi:10.1021/ja806520d.

[37] A.A. Sawyer, K.M. Hennessy, S.L. Bellis, Regulation of mesenchymal stem cell attachment and spreading on hydroxyapatite by RGD peptides and adsorbed serum proteins,

Biomaterials. 26 (2005) 1467–1475. doi:10.1016/j.biomaterials.2004.05.008.

[38] K. Kandori, M. Mukai, A. Yasukawa, T. Ishikawa, Competitive and cooperative adsorptions of bovine serum albumin and lysozyme to synthetic calcium hydroxyapatites, Langmuir. 16 (2000) 2301–2305. doi:10.1021/la9906424.

[39] K. Kandori, K. Murata, T. Ishikawa, Microcalorimetric study of protein adsorption onto calcium hydroxyapatites, Langmuir. 23 (2007) 2064–2070. doi:10.1021/la062562n.

[40] M.L. Wallwork, J. Kirkham, J. Zhang, D.A. Smith, Binding of matrix proteins to developing enamel crystals: an atomic force microscopy study, Langmuir. 17 (2001) 2508–2513. doi:10.1021/la001281r.

[41] M. Brundin, D. Figdor, G. Sundqvist, U. Sjögren, DNA binding to hydroxyapatite: A potential mechanism for preservation of microbial DNA, J. Endod. 39 (2013) 211–216. doi:10.1016/j.joen.2012.09.013.

[42] L.J. del Valle, O. Bertran, G. Chaves, G. Revilla-López, M. Rivas, M.T. Casas, J. Casanovas, P. Turon, J. Puiggalí, C. Alemán, DNA adsorbed on hydroxyapatite surfaces, J. Mater. Chem. B. 2 (2014) 6953–6966. doi:10.1039/C4TB01184H.

[43] K. Nakanishi, T. Sakiyama, K. Imamura, On the adsorption of proteins on solid surfaces, a common but very complicated phenomenon, J. Biosci. Bioeng. 91 (2001) 233–244. doi:10.1016/S1389-1723(01)80127-4.

[44] M. Mohsen-Nia, M. Massah Bidgoli, M. Behrashi, a. Mohsen Nia, Human Serum Protein Adsorption onto Synthesis Nano-Hydroxyapatite, Protein J. 31 (2012) 150–157. doi:10.1007/s10930-011-9384-3.

[45] D.T.H. Wassell, R.C. Hall, G. Embery, Adsorption of bovine serum albumin onto hydroxyapatite, Biomaterials. 16 (1995) 697–702. doi:10.1016/0142-9612(95)99697-K.

[46] E. Mavropoulos, A.M. Costa, L.T. Costa, C.A. Achete, A. Mello, J.M. Granjeiro, A.M. Rossi, Adsorption and bioactivity studies of albumin onto hydroxyapatite surface, Colloids Surfaces B Biointerfaces. 83 (2011) 1–9. doi:10.1016/j.colsurfb.2010.10.025.

[47] W. Norde, A.C.I. Anusiem, Adsorption, desorption and re-adsorption of proteins on solid surfaces, Colloids and Surfaces. 66 (1992) 73–80. doi:10.1016/0166-6622(92)80122-I.

[48] M. Rabe, D. Verdes, S. Seeger, Understanding protein adsorption phenomena at solid surfaces, Adv. Colloid Interface Sci. 162 (2011) 87–106. doi:10.1016/j.cis.2010.12.007.

[49] Q. Luo, J.D. Andrade, Cooperative adsorption of proteins onto hydroxyapatite, J. Colloid

Interface Sci. 200 (1998) 104–113. doi:10.1006/jcis.1997.5364.

[50] K.K. Kandori, A. Fudo, T. Ishikawa, Study on the particle texture dependence of protein adsorption by using synthetic micrometer-sized calcium hydroxyapatite particles, Colloids Surfaces B Biointerfaces. 24 (2002) 145–153. doi:10.1016/S0927-7765(01)00227-2.

[51] K. Kandori, H. Hamazaki, M. Matsuzawa, S. Togashi, Selective adsorption of acidic protein of bovine serum albumin onto sheet-like calcium hydroxyapatite particles produced by microreactor, Adv. Powder Technol. 25 (2014) 354–359. doi:10.1016/j.apt.2013.05.016.

[52] K. Kandori, M. Saito, H. Saito, A. Yasukawa, T. Ishikawa, Adsorption of protein on non-stoichiometric calcium-strontium hydroxyapatite, Colloids Surfaces A Physicochem. Eng. Asp. 94 (1995) 225–230. doi:10.1016/0927-7757(94)02969-5.

[53] E. Jimenez-Izal, F. Chiatti, M. Corno, A. Rimola, P. Ugliengo, Glycine adsorption at nonstoichiometric (010) hydroxyapatite surfaces: A B3LYP study, J. Phys. Chem. C. 116 (2012) 14561–14567. doi:10.1021/jp304473p.

[54] F. Chiatti, M. Corno, Y. Sakhno, G. Martra, P. Ugliengo, Revealing Hydroxyapatite Nanoparticle Surface Structure by CO Adsorption: A Combined B3LYP and Infrared Study, J. Phys. Chem. C. 117 (2013) 25526–25534. doi:10.1021/Jp4086574.

[55] G. Celotti, A. Tampieri, S. Sprio, E. Landi, L. Bertinetti, G. Martra, C. Ducati, Crystallinity in apatites: How can a truly disordered fraction be distinguished from nanosize crystalline domains?, J. Mater. Sci. Mater. Med. 17 (2006) 1079–1087. doi:10.1007/s10856-006-0534-7.

[56] A. Meldrum, L.M. Wang, R.C. Ewing, Electron-irradiation-induced phase segregation in crystalline and amorphous apatite: A TEM study, Am. Mineral. 82 (1997) 858–869. doi:https://doi.org/10.2138/am-1997-9-1003.

[57] L.. Wang, S.. Wang, R.. Ewing, A. Meldrum, R.. Birtcher, P. Newcomer Provencio, W.. Weber, H. Matzke, Irradiation-induced nanostructures, Mater. Sci. Eng. A. 286 (2000) 72–80. doi:10.1016/S0921-5093(00)00677-8.

[58] F. Catalano, G. Alberto, P. Ivanchenko, G. Dovbeshko, G. Martra, Effect of Silica Surface Properties on the Formation of Multilayer or Submonolayer Protein Hard Corona: Albumin Adsorption on Pyrolytic and Colloidal SiO2 Nanoparticles, J. Phys. Chem. C. 119 (2015) 26493–26505. doi:10.1021/acs.jpcc.5b07764.

[59] K. Rezwan, L.P. Meier, M. Rezwan, J. Vörös, M. Textor, L.J. Gauckler, Bovine serum

albumin adsorption onto colloidal Al2O3 particles: a new model based on zeta potential and UV-vis measurements., Langmuir. 20 (2004) 10055–61. doi:10.1021/la048459k.

[60] S. Beychok, Circular Dichroism of Biological Macromolecules, Science (80-.). 154 (1966) 1288–1299. doi:10.1126/science.154.3754.1288.

[61] W. Moffitt, J. Yang, The optical rotatory dispersion of simple polypeptides. I, Proc. Natl. Acad. Sci. U. S. A. 42 (1956) 596–603. doi:doi.org/10.1073/pnas.42.9.596.

[62] C.E. Giacomelli, W. Norde, The adsorption-desorption cycle. Reversibility of the BSA-silica system, J. Colloid Interface Sci. 233 (2001) 234–240. doi:10.1006/jcis.2000.7219.

[63] D.M. Charbonneau, H.A. Tajmir-Riahi, Study on the interaction of cationic lipids with bovine serum albumin, J Phys Chem B. 114 (2010) 1148–1155. doi:10.1021/jp910077h.

[64] C.E. Giacomelli, W. Norde, Influence of hydrophobic teflon particles on the structure of amyloid β-peptide, Biomacromolecules. 4 (2003) 1719–1726. doi:10.1021/bm034151g.